High-Reynolds Number Transitional Flow Prediction using a Coupled Discontinuous-Galerkin RANS PSE Framework

Gustavo Luiz Olichevis Halila*, Guodong Chen†, Yayun Shi‡
Krzysztof J. Fidkowski§, Joaquim R. R. A. Martins¶
University of Michigan, Aerospace Engineering Department. Ann Arbor, MI, 48109.

Márcio Teixeira de Mendonça‖
Instituto de Aeronáutica e Espaço, 12228-904 São José dos Campos, SP, Brazil.

The accurate prediction of transition is relevant for many aerodynamic analysis and design applications. Extending the laminar flow region over airframes is a potential way to reduce the skin friction drag, which in turn reduces fuel burn and greenhouse gas emissions. This paper introduces a numerical framework that allows for the inclusion of transition effects for high Reynolds number flows in a high-fidelity, Reynolds–Averaged Navier–Stokes (RANS) aerodynamic design framework. The CFD solver uses a discontinuous Galerkin (DG) finite element approach and includes goal-oriented adaptation. The Spalart-Allmaras (SA) turbulence model is used for the closure of the governing equations. In the flow stability analysis, the nonlocal, nonparallel effects that characterize boundary layers are accounted for by using the Parabolized Stability Equations (PSE). Transition onset is obtained through an e^N method based on the PSE calculations, while a smooth intermittency function allows for the inclusion of the transition region length. Numerical results for the NLF(1)-0416 airfoil present very good agreement with experimental data.

I. Introduction

Transition to turbulence is an important topic in fluid mechanics and impacts the performance of several engineering applications. Viscous drag has a major impact on fuel efficiency in modern commercial aircraft. Therefore, laminar flows are continuously investigated in the aerospace industry as a tool for increasing overall airplane efficiency, with potential benefits in direct operational costs. In addition, the correct estimation of drag and lift coefficients depends on the precise calculation of the laminar regions in the airframe.

In typical aerospace configurations, several mechanisms can trigger transition to turbulence. The amplification of unstable Tollmien-Schlichting (TS) waves usually causes transition in wings with low sweep angles. In the transonic flow regime, wings with high sweep angles are commonly affected by transition caused by crossflow (CF) vortices. Two types of CF instabilities exist: stationary CF vortices and traveling CF waves. From the physical point of view, these two different families of modes are generated by distinct receptivity mechanisms.[1] While stationary CF vortices are excited by surface variations (surface polishing or suction), traveling CF waves are triggered by an unsteady source, such as freestream turbulence.[2] Only for turbulence levels $Tu > 0.2\%$ and smooth surfaces do the traveling instability waves dominate.[3] Laminar separation bubbles (LSB) can cause transition in separated flows. Reattachment may take place since turbulent boundary layers are more resistant to adverse pressure gradients than laminar ones. Leading-edge attachment line contamination occurs when the turbulent boundary layer of the fuselage runs onto the leading edge of a swept wing, resulting in the loss of laminar flow over the wing.[4] In addition, attachment line transition takes place if disturbances are amplified in the leading edge region. This happens depending on the flow and leading edge geometry.

*Ph.D. candidate; E-mail: ghalila@umich.edu.
†Ph.D. candidate.
‡Visiting Scholar.
§Associate Professor. AIAA Senior Member.
¶Professor. AIAA Associate Fellow.
‖Senior Research Engineer, Aerospace Propulsion Division, Departamento de Ciência e Tecnologia Aeroespacial, DCTA/IAE/APA.

In the last few decades, different tools have been proposed to consider transitional flow effects in computational fluid dynamics (CFD). Simplified methods include database methods and analytic criteria. The latter consider information deduced from experimental data, while the former rely on the disturbance growth computation based on tabulated values or based on analytic relations obtained from exact stability calculations which are, in general, performed over self-similar velocity profiles.[2] These methods have been first proposed by Gaster and Jiang (1994),[5] van Ingen (1996),[6] and Stock (1996).[7] Other examples of database methods are the neural network framework presented by Crouch [8] and the three-parameter database approach used by Drela[9] in a coupled inviscid-viscous flow solver.

Reynolds–Averaged Navier Stokes (RANS) turbulence models, which are commonly used in engineering applications, can be seen as the result of a Favre time-averaging of the original Navier– Stokes equations. As a result, important spectral information is missing.[10] The natural approach to overcome such a difficulty is the development of an extra model for the transitional region and its integration into the original turbulence closure. Modeling of transition to turbulence is performed through the inclusion of additional transport equations, generally by adopting an intermittency field. At present, such modified RANS models can account for different transition mechanisms, and the specification of boundary conditions for turbulent variables has strong effects on the correct prediction of transitional flows over typical aerospace configurations.[11] A detailed review of RANS-based transition analysis is provided by Pasquale et al. [12].

Large Eddy Simulations (LES) can also be used as a tool to study transitional flows. By solving for the large eddies and modeling the small ones, the technique can be employed to study low-Reynolds, transitional flows. For instance, Uranga et al. [13] performed the simulation of the transitional flow around an airfoil based on the Implicit LES (ILES)approach, using a discontinuous Galerkin (DG) method. Fernandez et. al. [14] extended the use of the ILES technique for transitional flows to a hybridized DG (HDG) method and considered flows over aeronautical and compressor cascade airfoils with Reynolds numbers up to $460,000$. As of now, the use of LES approaches is computationally limited to low and moderate Reynolds numbers.

Direct Numerical Simulation (DNS) is the highest-fidelity approach in the numerical description of fluid flow. In fact, DNS methods can be used to accurately simulate laminar flow breakdown, the development of turbulent spots, and transition to fully-developed turbulent flow.[15] Since eddies down to the the Kolmogorov scale are directly resolved, stringent requirements are imposed in the mesh size. No additional turbulence modeling or closure assumptions are necessary. As a result, DNS calculations are very expensive and, at present, they are not used for industry-relevant aerodynamic configurations.

Stability analysis is a mathematical tool that identifies the growth and decay of certain modes in fluid flows. Unstable amplification of modes leads to instability and the eventual onset of a fully-turbulent state. Typically, the instability of flows to small amplitude perturbations is analyzed using the modal approach,[16] and both temporal and spatial problems can be considered. The oldest method to characterize boundary layer instabilities is based on the linear Orr-Sommerfeld equation[2] (OSE) and represents a local, parallel analysis. This method is usually referred to as Linear Stability Theory (LST), even though there are other linear stability analysis tools that do not consider local and parallel baseflows. LST has been widely used to study transition to turbulence and a comprehensive review can be found in the literature.[17] Its main shortcoming is the fact that the boundary layer growth is not considered. Also, nonparallel effects are not included in the formulation and curvature effects cannot be accounted for.

A nonlocal, nonparallel stability analysis can be used to take into account both nonparallel and history effects, both relevant in boundary layer flows. One example of this approach are the Parabolized Stability Equations (PSE) [18,19,20]. This method allows for the study of the convectively-unstable waves evolution in boundary-layer flows. Both TS and CF instabilities can be considered. The computational cost is of the same order as the one for the traditional LST approach.[2] The possibility of including important physical aspects to the analysis at an affordable computational cost makes the PSE an ideal tool for transition prediction, and some recent studies[21] highlight the relevance of using PSE for transition analysis over general aerospace configurations. A complete review of the use of stability analysis tools for transition prediction is available in Ref. [22]. For transition purposes, the use of linear tools, in which the disturbances amplitudes are infinitesimally small, is an efficient approach.

By using the PSE method, growth rates can be obtained for disturbances superimposed to a given baseflow. The growth rates integration leads to an N-factor that can then be used to predict the onset of the transition region, as first proposed by van Ingen.[23] A smooth, continuous intermittency function can be used to estimate the transition region extent. The resulting information for the transition front and transition length is then used to select regions of laminar and turbulent flow within a RANS framework.

Previous work[24] demonstrated the successful integration of an LST method for transition prediction with a finite-volume RANS solver. In the present paper, we introduce effects of transition to turbulence as predicted by a PSE capability into a discontinuous Galerkin CFD code that solves a RANS formulation and includes goal-oriented adap-

tation. In contrast to other publications that used an ILES approach to handle transitional flows with a DG method,[13,14] our implementation targets high Reynolds numbers that are more representative of large aircraft configurations. We present results for the NLF(1)-0416 airfoil for which a vast amount of experimental of data is available in Ref. [25].

The inclusion of transition to turbulence based on the PSE approach in an optimization capability will enable us to perform aerodynamic shape optimization including laminar flow regions and it is the next stage of the present research project. High-fidelity aerodynamic optimization is now a very active research field with industrial applications. The evolution of this topic can be traced back to the work of Hicks et al. [26], in which the airfoil optimization problem was considered. The use of the adjoint method in fluid mechanics was first introduced by Pironneau,[27] who derived the adjoint of the Stokes equations and of the Euler equations.[28] Jameson extended the method to inviscid compressible flows[29] making it suitable for transonic airfoil design. At present, complex aircraft configurations are optimized considering high-fidelity, RANS-based CFD calculations. As an example, Lyu et al. [30] were able to perform the lift-constrained drag minimization of the NASA Common Research Model (CRM) wing with a RANS turbulence model. The corresponding wing-body-tail configuration was also optimized by Chen et al. [31]. In a DG CFD solver, aerodynamic shape optimization using output-based adapted meshes has also been performed.[32]

II. Governing Equations and Discretization

II.A. Discontinuous Galerkin Finite-Element Method

The equations governing the fluid flow system in this work can be written in conservative form as

$$\frac{\partial \mathbf{u}}{\partial t} + \nabla \cdot \vec{\mathbf{F}}(\mathbf{u}, \nabla \mathbf{u}) + \mathbf{S}(\mathbf{u}, \nabla \mathbf{u}) = \mathbf{0}. \tag{1}$$

This general form encompasses scalar advection-diffusion-reaction and the compressible Navier–Stokes equations. For the latter, $\mathbf{u}$ is the conservative state vector composed of the flow variables, $\vec{\mathbf{F}}$ denotes the total inviscid and viscous flux vectors, and $\mathbf{S}$ represents the source term required when modeling turbulence. When running Reynolds-averaged turbulent cases, we use the Spalart-Allmaras (SA) one-equation model, with a negative turbulent-viscosity modification.[33]

We discretize Eq. [1] with the discontinuous Galerkin (DG) finite-element method, which is suitable for high-order accuracy and hp-refinement.[34,35,36] The computational domain Ω is divided into a shape-regular mesh $\mathcal{T}_h$ consisting of N_e non-overlapping elements Ω_e, $\mathcal{T}_h = \{\Omega_e : \bigcup_{e=1}^{Ne} \Omega_e = \Omega, \bigcap_{e=1}^{Ne} \Omega_e = \emptyset\}$. In DG, the state components are approximated by piece-wise polynomials in the approximation space $\mathcal{V}_h^p$, with no continuity constraints imposed on the approximations between adjacent elements. The approximation space consists of element-wise polynomials and is defined as $\mathcal{V}_h^p = \{v_h \in L^2(\Omega) : v_h|_{\Omega_e} \in \mathcal{P}^{p_e}, \forall \Omega_e \in \mathcal{T}_h\}$, where $\mathcal{P}^{p_e}$ denotes polynomials of order p_e on element Ω_e, a distribution that is not necessary uniform throughout the mesh. The weak form of Eq. [1] follows from multiplying the equation by test functions (taken from the approximation space), integrating by parts, and coupling elements via unique inter-element fluxes. We use the Roe approximate Riemann solver[37] for the inviscid flux, and the second form of Bassi and Rebay (BR2) for the viscous flux.[38] Choosing a basis for the test and trial spaces yields a system of nonlinear, algebraic equations,

$$\mathbf{R}_H(\mathbf{U}_H, \mathbf{x}) = \mathbf{0}, \tag{2}$$

where, $\mathbf{R}_H$ is the discrete residual vector, a nonlinear function of the discrete state vector $\mathbf{U}_H$ and the design variables $\mathbf{x}$. For the steady state problems considered in this work, $\mathbf{R}_H$ is the discrete spatial residual vector. The subscript H refers to the discretization fidelity of the approximation/test space with respect to the approximation order and mesh refinement.

II.B. Modal Linear Stability Analysis

In the stability analysis approach, the overall principle is based on the decomposition of any flow property $\mathbf{q}$ into a steady base state $\bar{\mathbf{q}}$ and an unsteady perturbation component, $\tilde{\mathbf{q}}$, as follows:

$$\mathbf{q}(\mathbf{x}, t) = \bar{\mathbf{q}}(\mathbf{x}) + \epsilon \tilde{\mathbf{q}}(\mathbf{x}, t), \tag{3}$$

where $\mathbf{x}$ is the space coordinate vector, t is the time, and $\mathbf{q} = (\rho, u, v, w, T)$ is the flow state vector. We further observe that, as long as we consider the linear stability problem, the perturbations have small amplitudes such that $\epsilon \ll 1$. When such an *ansatz* is applied to the Navier–Stokes equations, a linearization is performed by neglecting terms of $\mathcal{O}(\epsilon^2)$ and $\mathcal{O}(\epsilon^3)$. The equations for the steady flow, which also respect the Navier–Stokes equations, are subtracted,

and one obtains the linearized perturbation equations, referred to as the *Linearized Navier–Stokes equations*, LNSE. The LNSE can be written as an initial value problem. If the baseflow $\bar{\mathbf{q}}$ is steady, time and space dependencies can be split in this equation. This allows for the introduction of a Fourier decomposition in time by means of the relation $\tilde{\mathbf{q}} = \hat{\mathbf{q}}\exp(-i\omega t)$, with ω the angular frequency. Naturally, the linearization introduced in the Navier–Stokes equations, leading to the LNSE, is only valid when the disturbance amplitude remains small such that the non-linear terms are negligible. Indeed, the real, nonlinear system might present an unstable behavior if finite-amplitude disturbances are considered, under conditions in which the linearized system remains stable.

In modal linear stability analysis, the perturbation term is written as the product of an amplitude $\hat{\mathbf{q}}$ and a phase function Θ:

$$\tilde{\mathbf{q}} = \hat{\mathbf{q}}e^{i\Theta}. \tag{4}$$

Different stability methods are based on distinct assumptions regarding the topology of the baseflow $\bar{\mathbf{q}}$ and the fluctuation $\tilde{\mathbf{q}}$. The overall differences between LST (Orr-Sommerfeld) and PSE methodologies are presented in Table [1]. In Table [1], $\alpha = 2\pi/L_x$ is the streamwise wave number, $\beta = 2\pi/L_z$ is the spanwise wave number, with L_x and

Table 1: General classification of modern stability analysis theory.[16]

Method	Assumption	Baseflow	Amplitude Function	Phase Function Θ
PSE	$\partial_x\bar{\mathbf{q}} \ll \partial_y\bar{\mathbf{q}}; \partial_z\bar{\mathbf{q}} = 0$	$\bar{\mathbf{q}}(x^*, y)$	$\hat{\mathbf{q}}(x^*, y)$	$\int \alpha(x')dx' + (\beta z - \omega t)$
LST	$\partial_x\bar{\mathbf{q}} = \partial_z\bar{\mathbf{q}} = 0$	$\bar{\mathbf{q}}(y)$	$\hat{\mathbf{q}}(y)$	$\alpha(x) + (\beta z - \omega t)$

L_z the wavelengths in the streamwise (x) and spanwise (z) directions, respectively. Also, ω is the angular frequency, and x^* represents the slow variation of the baseflow properties in the streamwise direction. The wall-normal direction is denoted by y.

The first flow stability studies focused on flows in which inhomogenity is observed in only one spatial direction. This is the case of a channel flow in which the baseflow only presents variations in the wall-normal direction. In this specific case, $\partial_x\bar{\mathbf{q}} = \partial_z\bar{\mathbf{q}} = \mathbf{0}$, and $\bar{\mathbf{q}}(\mathbf{x}) = \bar{\mathbf{q}}(y)$. Such approximations are valid for parallel flows, such as Couette and Pouiseuille flows.[39] The introduction of a Fourier decomposition along the streamwise, x, and the spanwise, z, directions may be written to derive different variations of the Orr–Sommerfeld equations.[40]

Boundary-layer flows are characterized by two inhomogeneous spatial directions, with the baseflow depending both on streamwise and normal coordinates, with slow variations in the streamwise direction, i.e., $\partial_x\bar{\mathbf{q}} \ll \partial_y\bar{\mathbf{q}}$. To solve such a type of flow, the Parabolized Stability Equations (PSE) method was first introduced by F. Bertolotti and T. Herbert [41, 18, 19]. In contrast to the eigenvalue problem represented by the Orr–Sommerfeld equations, the PSE technique solves the stability problem by integrating the LNSE, via a marching procedure, along the streamwise direction. The initial values for the eigenfunctions $\hat{\mathbf{q}}$ and the streamwise wavenumber (α) are obtained from a local stability analysis performed in the first streamwise station. Comprehensive reviews of the PSE method can be found in references [42] and [20].

II.C. PSE Theoretical Formulation

The PSE technique aims at representing baseflows in which variations in the streamwise direction are much smaller than those in the wall-normal direction. Mathematically, this can be expressed as

$$\partial_x\bar{\mathbf{q}} \ll \partial_y\bar{\mathbf{q}}; \quad \partial_z\bar{\mathbf{q}} = \mathbf{0}, \tag{5}$$

$$\bar{\mathbf{q}}(\mathbf{x}) = \bar{\mathbf{q}}(x^*, y), \tag{6}$$

where x^* is a scaled version of x used to represent the slow variation of the baseflow in the x direction. From the baseflow assumptions, it follows that the PSE method is well-adapted to the prediction of flows such as boundary layers, jets, wakes, and mixing layers when high Reynolds numbers are considered. The important aspect to observe is that the PSE methodology is valid for convectively unstable flows.

The baseflow velocity components $\bar{u}$ and $\bar{v}$, aligned with the streamwise and spanwise directions, respectively, exhibit small variations in the streamwise (x) direction and are constant along the spanwise (z) direction. We introduce the local Reynolds number, $Re = U_e\delta(x)/\nu$ with ν the kinematic viscosity and $\delta(x)$ a characteristic length scale proportional to the boundary layer thickness, $\delta(x) = \sqrt{\nu x/U_e}$, with U_e the unperturbed edge velocity. The wall-normal component, $\bar{w}$, is nonzero and scales with $1/Re$. Formally defining the slowly varying scale $x^* = x/Re$, the

scaling are:

$$\begin{aligned} \bar{w} &\sim \frac{1}{Re}, \\ \frac{\partial}{\partial x^*} &\sim \frac{1}{Re}, \\ \alpha &= \alpha\left(x^*\right), \\ \hat{\mathbf{q}} &= \hat{\mathbf{q}}\left(x^*, y\right). \end{aligned} \tag{7}$$

With these scaling in mind, one can observe that $\epsilon \sim 1/Re$.

The perturbation vector is expanded in terms of its truncated Fourier components assuming time-periodicity,

$$\tilde{\mathbf{q}}(x, y, x, t) = \sum_{m=-M}^{M} \sum_{n=-N}^{N} \breve{\mathbf{q}}_{m,n}(x, y) \exp\left[i\left(m\beta z - n\omega t\right)\right], \tag{8}$$

where $\breve{\mathbf{q}}$ represents the fast varying wave function with a slowly-varying amplitude $\hat{\mathbf{q}}(x, y)$:

$$\breve{\mathbf{q}}_{m,n}(x, y) = \hat{\mathbf{q}}_{m,n}(x, y) \exp\left[i \int_x \alpha_n\left(x'\right) dx', \right] \tag{9}$$

and $\hat{\mathbf{q}}(x, y)$ has a slow variation in x. If a linear approach is considered, only one mode for each spanwise direction and time is needed. Using the PSE approximation, it follows that the streamwise (in the x-direction) derivatives of the amplitude $\breve{\mathbf{q}}$ are expressed as

$$\frac{\partial \breve{\mathbf{q}}}{\partial x} = \left(i\alpha\hat{\mathbf{q}} + \frac{\partial \hat{\mathbf{q}}}{\partial x}\right) \exp\left[i \int_x \alpha\left(x'\right) dx'\right], \tag{10}$$

$$\frac{\partial^2 \breve{\mathbf{q}}}{\partial x^2} = \left(-\alpha^2\hat{\mathbf{q}} + 2i\alpha\frac{\partial \hat{\mathbf{q}}}{\partial x} + i\frac{d\alpha}{dx}\hat{\mathbf{q}}\right) \exp\left[i \int_x \alpha\left(x'\right) dx'\right]. \tag{11}$$

Finally, by replacing equations [9], [10], and [11] in the LNSE, neglecting terms of $\mathcal{O}(\epsilon^2)$, and considering the scaling from Eq. [7], as well as dropping higher derivatives with respect to x or streamwise derivatives in the viscous terms (noting that $\frac{\partial}{\partial x}\frac{1}{Re} \sim \epsilon^2$), the linear PSE equations are written in compact form as

$$\mathbf{A}\hat{\mathbf{q}} + \mathbf{B}\frac{1}{h_y}\frac{\partial \hat{\mathbf{q}}}{\partial y} + \mathbf{C}\frac{1}{h_y^2}\frac{\partial^2 \hat{\mathbf{q}}}{\partial y^2} + \mathbf{D}\frac{1}{h_x}\frac{\partial \hat{\mathbf{q}}}{\partial x} = \mathbf{0}. \tag{12}$$

The effects of geometry curvature over the disturbances are accounted for by the stretching factors, h_x and h_y. The entries for the compressible PSE operators **A**, **B**, **C**, and **D** can be found in Ref. [43]. The boundary conditions are as follows:

$$\hat{u} = \hat{v} = \hat{w} = \hat{T} = 0 \quad \text{at} \quad y = 0, \tag{13}$$

$$\hat{u} = \hat{v} = \hat{w} = \hat{T} \to \infty \quad \text{as} \quad y \to \infty. \tag{14}$$

In the PSE framework, changes in amplitude along the slow spatial direction can be contained both in the amplitude function $\hat{\mathbf{q}}$ or in the phase function defined in Eq. [9]. To remove such ambiguity, a normalization condition is required. One possibility for the normalization is imposing

$$\int_0^\infty \hat{\mathbf{u}}^\dagger \frac{\partial \hat{\mathbf{u}}}{\partial x} dy = 0, \tag{15}$$

where the superscript † represents the complex conjugate. By using the normalization condition proposed in Eq. [15], one enforces that all fast variations in the streamwise direction (x) are, up to a given acceptable level (such that the equality in Eq. [15] is close to zero), absorbed into the phase function, such that the scaling of $(1/Re)$ in $\partial\hat{\mathbf{q}}/\partial x$ is valid.

The physical growth of an arbitrary disturbance ξ can be defined as[16]

$$\sigma = \frac{1}{h_x}\left(-\alpha_i + \Re\left[\frac{1}{\xi}\frac{\partial \xi}{\partial x}\right]\right), \tag{16}$$

where the subscript i indicates the imaginary part. The disturbance kinetic energy is used to measure the disturbance growth,

$$E(x) = \int_0^\infty \left(|\hat{\mathbf{u}}|^2 + |\hat{\mathbf{v}}|^2 + |\hat{\mathbf{w}}|^2 \right) dy, \tag{17}$$

and, hence, equation (16) becomes:

$$\sigma_E = \frac{1}{h_x} \left(-\alpha_i + \frac{1}{2} \frac{d}{dx} \ln \left[E(x) \right] \right). \tag{18}$$

The set of equations represented in Eq. [12] is intended to be parabolic. Therefore, it is possible to treat the streamwise direction, x, as a pseudo-time and then to implement a marching strategy in this spatial direction. Numerical instabilities appear when the streamwise integration step is too small.[16] The reason for that, as explained by Herbert,[20] is that there are traces of ellipticity that inject ill-posed characteristics. One remedy for this is the use of a first-order backward difference scheme with a lower integration step limit $\Delta x > 1/|\alpha_r|$. To relax this limit, Andersson et. al. [44] propose an stabilization procedure leading to $\Delta x > 1/|\alpha_r| - 2s$, where s is a small number.

Due to the predominantly parabolic character of Eq. [12], the disturbance evolution is influenced by both local and upstream flow conditions. Therefore, the parabolized stability equations are recognized as a *nonlocal* method, in contrast to, for instance, the *Orr-Sommerfeld* equation that is a *local* approach. For three-dimensional flows, there are some possibilities for the marching direction. Using an orthogonal coordinate system, the most usual approach consists in orienting the streamwise direction towards a normal to the leading edge, the spanwise direction being parallel to the leading edge. Another choice would be perform a marching that follows the inviscid streamline. A complete discussion on suitable marching directions is available in the literature.[45,21] Another relevant aspect to be considered when using PSE is the starting integration point. It is necessary to place this point some flow stations upstream of the neutral point location. A deeper discussion on this issue is available in Ref. [46]

III. Transition Prediction

III.A. N-factor and Transition Region Beginning

The beginning of the transition region can be determined based on an e^N method. The amplification factor or N-factor is defined as

$$N = \ln \left(\frac{A}{A_0} \right) = \int \sigma_E \left(x \right) dx, \tag{19}$$

with A_0 the disturbance amplitude at the first neutral-stability point. The N-factor envelope is obtained by running the PSE code using several frequencies and spanwise wave numbers and superimposing the resulting N-factor curves at each station during the PSE solve.

The position in which the transition region starts, $x_{TR,\text{beg}}$, is allowed to be in between two cells by using a simple linear interpolation that considers the two mesh points in between which the N-factor envelope satisfies the threshold value for the amplification factor, usually called critical amplification or critical N-factor. This leads to the following expression for the transition location,

$$x_{TR,\text{beg}} = \frac{\left(N_R - N_{\text{crit}} \right) x_L + \left(N_{\text{crit}} - N_L \right) x_R}{\left(N_R - N_{\text{crit}} \right) + \left(N_{\text{crit}} - N_L \right)}, \tag{20}$$

where x_L and x_R are, respectively, the left and right neighbors of the position where N_{crit} is reached and N_L and N_R are the corresponding N-factor values. The critical value for the N-factor, N_{crit}, can be obtained from experimental data. For some transition mechanisms, empirical correlations are available. For Tollmein-Schlichting waves, Mack[47] suggested the following empirical correlation relating the critical N-factor to the turbulence level, Tu,

$$N_{\text{crit,TS}} = -8.43 - 2.4 \ln \left(Tu \right). \tag{21}$$

This correlation is valid for $0.001 < Tu < 0.01$, and sometimes is also used to indicate critical values for crossflow (CF) vortices, as in Ref. [21]. Since flow stability tools only provide the transition region starting point (transition onset), additional correlations are used to estimate the length of the transition region. Our framework also includes correlations that allow for the prediction of transition triggered by flow separation through laminar separation bubbles (LSB) and leading edge transition and contamination, as it is further discussed in Ref. [24].

III.B. Intermittency Function and Interaction with the Spalart-Allmaras Turbulence Model

Physically, the intermittency indicates the probability of a flow location to be turbulent. We use a smooth intermittency function to generate the transition region in a RANS computation framework. This function reads

$$\gamma = 1 - \exp^{-0.413\xi^2}, \tag{22}$$

where

$$\xi = \frac{3.36\left(s - s_{tr}^{\text{beg}}\right)}{\left(s_{tr}^{\text{end}} - s_{tr}^{\text{beg}}\right)}, \tag{23}$$

with s the arc length measured from the stagnation point. In Eq. [23], the superscripts beg and end refer to the beginning and end of the transition region, respectively. The ending arc point, s_{tr}^{end}, is determined based on the correlation below,[48]

$$s_{tr}^{\text{end}} = 2.3\sqrt{\frac{U_e}{\nu_e}}\left(\delta_1\right)^{1.5} + s_{tr}^{\text{beg}}, \tag{24}$$

where U_e and ν_e are the velocity and kinematic viscosity at the boundary layer edge, respectively, and δ_1 is the boundary layer displacement thickness. All these quantities are evaluated at the flow position corresponding to s_{tr}^{beg}.

The intermittency function γ is used as a factor of both production and destruction terms in the SA turbulence model such that the eddy viscosity production is suppressed in laminar regions.[49] The governing equation for the SA model[33] working variable, $\tilde{\nu}$, is then modified and reads

$$\frac{D\tilde{\nu}}{Dt} = \gamma P - \gamma_{\text{lim}} D + T + \frac{1}{\sigma}\left[\nabla\cdot\left(\left(\nu+\tilde{\nu}\right)\nabla\tilde{\nu}\right) + c_{b2}\left(\nabla\tilde{\nu}\right)^2\right], \tag{25}$$

where P and D are, respectively, the production and destruction terms and γ_{lim} reads[50]

$$\gamma_{\text{lim}} = min\left[max\left(\gamma, 0.1\right)1.0\right]. \tag{26}$$

A deeper discussion of the other variables in Eq. [25] can be found in Ref. [33].

III.C. Transition Module Coupling with CFD Solver

The interaction between the CFD and the transition module, that is able to perform both LST and PSE analyses, is illustrated in Fig. [1]. The laminar baseflow can be obtained using two different approaches. Our conical boundary

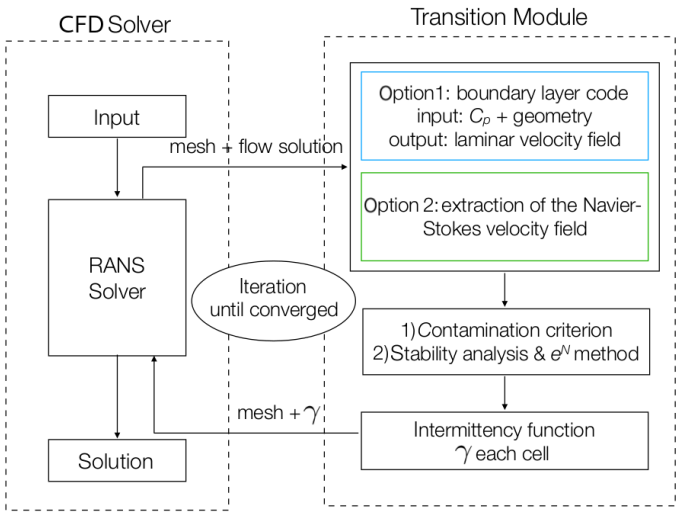

Figure 1: Workflow for the transition prediction capability, adapted from Ref. [24].

layer code can be used to provide the laminar flow field given a pressure coefficient (c_p) distribution. It is also possible to extract the baseflow from the CFD solver itself. A set of suitable waves is then provided by our LST code. These

waves, along with baseflow information, are then sent to the PSE capability, which provides the transition onset point. The intermittency function shown in Eq. [22] is then prescribed to all mesh elements such that the turbulence model can allow for laminar, transitional, and turbulent regions. This process is iterative. For flows that are shock wave-free or in which these are weak, the iterative process might not be necessary as the c_p distribution is not strongly affected by including transition and, as a result, the transition location does not present significant variations during the iterative process. If moderate to strong shock waves are present, then the transition location will only converge after iterating as indicated in Fig. 1.

IV. PSE Verification

Our compressible PSE tool is able to advance the PSE solution using both first and second-order implicit schemes and considers 2 and 2.5-D baseflows with uniform or nonuniform meshes. The stabilization procedure suggested in Ref. [44] is also included in the implementation. A growing mesh that emulates the boundary layer growth is included as an option. The normal to the wall direction is discretized using a spectral method based on the Chebyshev collocation points with a suitable mapping to the computational domain, with point clustering close to the wall and boundary layer edge for high-speed flows. The curvature metrics highlighted in Sec. [II.C] are also included in the current implementation. Curvature effects are also introduced in the baseflow quantities inside the PSE operators. The first streamwise position is solved using a local method based on the PSE operators without the nonparallel terms. The resulting eigenfunctions are then used as starting values for the PSE marching.

IV.A. Subsonic and Supersonic Flat Plate Test Cases

To verify the compressible PSE implementation, two flat plate test cases are performed: low and high Mach number flows. In both cases, results are compared to those obtained with the NOLOT code, which is a linear, compressible PSE implementation.[43] Our PSE code is named StabFlow.

For the low Mach number test case, we select a constant, dimensionless reduced frequency $F = 1.4 \times 10^{-4}$. The reduced frequency is related to the dimensional frequency, f, according to $F = 2\pi f \left(\nu/U_e^2\right)$. The Mach number is $M = 0.01$ and the marching ranges from $Re_\delta = 100$ to $Re_\delta = 650$, Re_δ being the Reynolds number based on the Blasius characteristic length variable. The freestream temperature is $T = 299$ K and the Prandtl number is $Pr = 0.71$. For this test case, the waves are aligned with the streamwise direction ($\beta = 0$). For this simulation, 60 Chebyshev points are used in the wall-normal direction. The results for the energy-based growth rate, σ_E, can be seen in Fig. 2. The agreement between the benchmark code (NOLOT) and our implementation (StabFlow) is good for both growing

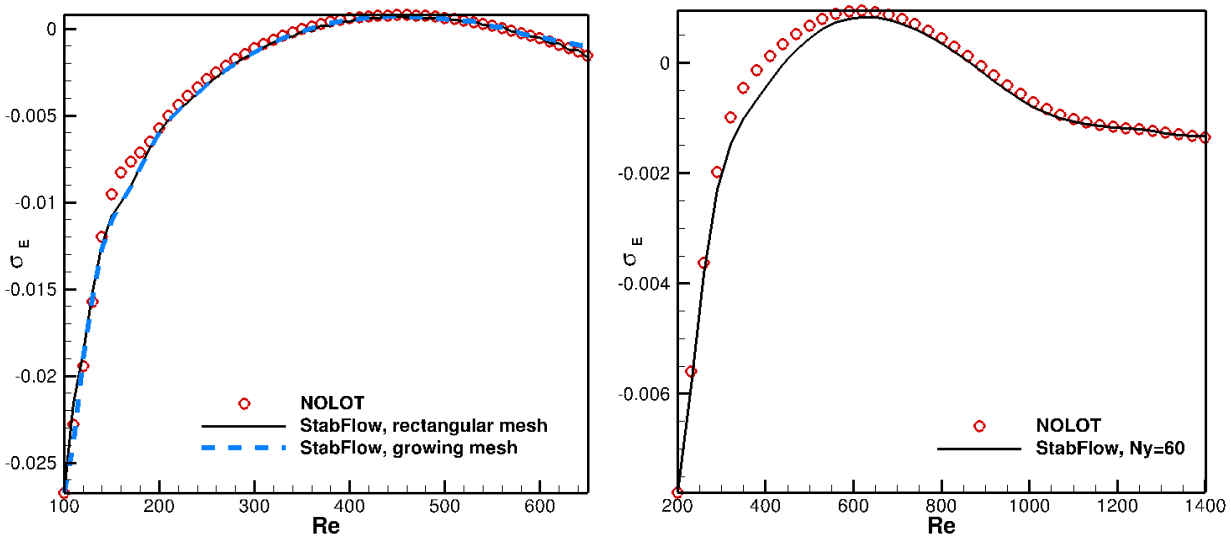

(a) M=0.01 (b) M=1.6

Figure 2: Energy-based growth rates for subsonic (left) and supersonic (right) flow over a flat plate.

and rectangular meshes.

A numerical simulation considering supersonic flow at $M = 1.6$ over a flat plate is considered. The freestream temperature is $T = 300$ K and the Prandtl number is $Pr = 0.71$. For this specific test case, we choose an oblique wave with $\beta/R = 1.52 \times 10^{-4}$ and a reduced frequency $F = 5.0025 \times 10^{-5}$. The marching extends from $Re_\delta = 200$ to $Re_\delta = 1400$ with a step of $\Delta Re_\delta = 30$. The simulation is converged for 60 Chebyshev points in the wall-normal direction. The results for the energy-based growth rate, σ_E, are depicted in Fig. 2. Once again, the results are in good agreement with the NOLOT data. Some transient effects appear in the early marching stations and vanish afterwards.

To inspect the eigenfunctions, we observe the wave amplitudes for the three velocity components, temperature, and density at the marching mid-station. The results are illustrated in Fig. 3. The wall-normal perturbation velocity decay is

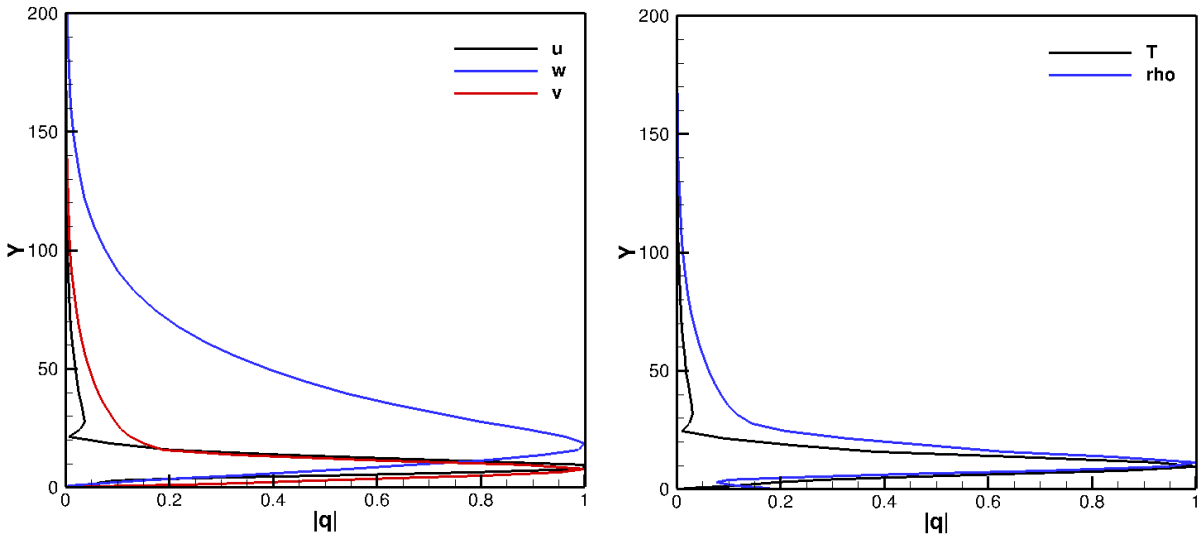

(a) Perturbation velocity components

(b) Perturbation temperature and density components

Figure 3: Normalized, absolute values of eigenfunctions in the mid-station for flow at $M = 1.6$ over a flat plate.

the one that requires a larger computational domain, as can be seen in Fig. 3. For this reason, the computational domain should be as large as 100 to 200 times the local reference length at each marching station if TS waves are included. Crossflow instabilities, on the other hand, decay faster in the freestream and a smaller computational domain can be considered.

IV.B. NACA 0012 Airfoil

We use a NACA 0012 airfoil at a zero angle of attack, M=0.1, and chord-based Reynolds number of 1, 3, 5, 8, and 15 million to further investigate our PSE implementation with transition prediction. As there are no experimental results for this specific set up, we compare our results to those obtained with our LST capability, which was extensively validated against experimental data in Ref. [24]. This is a valid test since TS waves are not largely affected by curvature, nonlocal, and nonparallel effects, that are not accounted for in the LST formulation.

Figure [4] shows the N-factor envelopes for all of the Reynolds numbers mentioned above. The critical N factor, $N_{\text{crit},TS} = 8.14$ is also represented. This critical N-factor was obtained by using Eq. [21] for a turbulence level of $Tu = 0.1\%$. Figure [4] also indicates the beginning and end chord locations for the transition region for all 5 flight conditions addressed here. Since the NACA0012 airfoil is symmetric and we use a zero angle of attack, we only display results for the suction side of the airfoil. We observe that, with increasing freestream Reynolds number, the transition front moves upstream and the transition region becomes shorter than for smaller freestream Reynolds numbers, indicating that the model is able to reproduce the fact that, for higher Re numbers, the evolution of the flow structures that lead to turbulent flow are faster than for lower Reynolds flows.

The results for the beginning of the transition location for the NACA 0012 test cases are illustrated in Table [2]. Agreement between both flow stability analysis implementations is very good for all of the Reynolds numbers considered here.

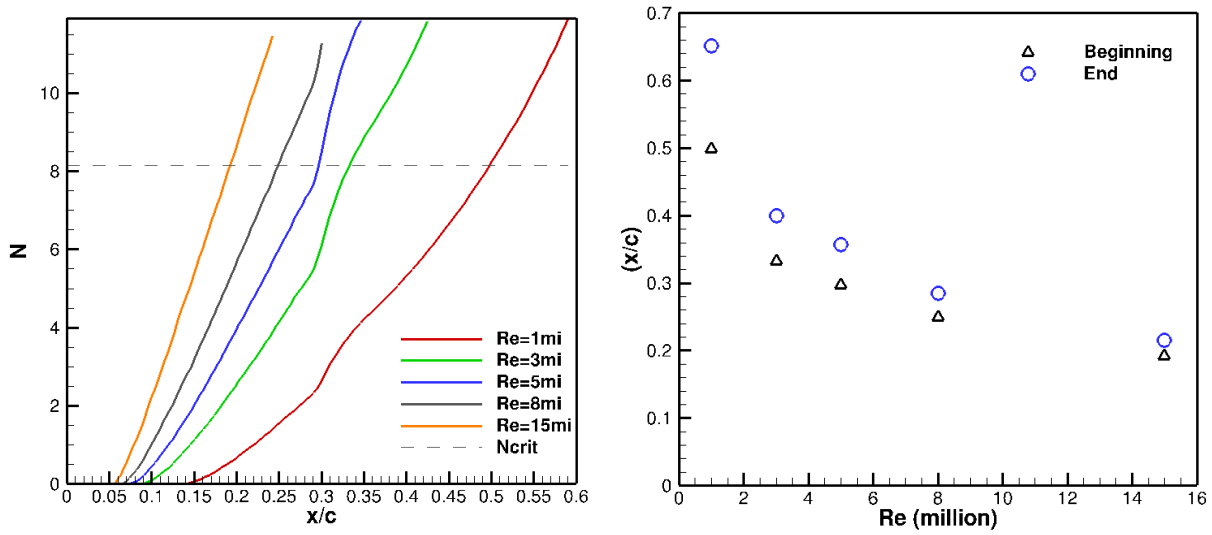

(a) N-factor envelopes

(b) Transition location

Figure 4: N-factor envelopes (left) and transition locations (right) for a NACA 0012 airfoil at multiple Reynolds numbers.

Table 2: NACA 0012 airfoil transition information for different Re numbers.

Re (million)	PSE, $(x/c)_{tr}$	LST, $(x/c)_{tr}$	Percent Error
1	0.498	0.493	0.87
3	0.333	0.349	0.74
5	0.297	0.296	0.39
8	0.249	0.246	1.11
15	0.192	0.191	0.56

IV.C. NLF(1)-0416 Airfoil

The Natural Laminar Flow NLF(1)-0416 airfoil is a general aviation airfoil largely tested at the NASA Langley Low-Turbulence Pressure Tunnel (LTPT).[25] Turbulence intensity measurements in the LTPT wind tunnel indicate that it is a very quiet test apparatus.[51] However, Ref. [49] mentions that the original turbulence intensities for this wind tunnel might not lead to good agreement with experimental data when used along with transition modeling tools. Therefore, we choose $Tu = 0.1\%$ for this test case. As a result, the critical N-factor is $N_{\text{crit,TS}} = 8.14$ as suggested by Eq. [21].

We select two flight conditions, depicted in Table [3]. According to Ref. [25], transition is triggered by amplification of TS waves in the suction side of the airfoil for both of these flight conditions.

Table 3: NLF(1)-0416 flight conditions.

Condition	Re (million)	M	Angle of attack (degrees)
1	4	0.1	0.0
2	2	0.1	4.0

For flight condition 1, our transition prediction framework considers a set of TS waves with frequencies ranging from 1100 to 2400 Hertz for the suction side of the airfoil, and from 580 to 2000 Hertz for the pressure side. For flight condition 2, the frequencies range from 1060 to 3000 Hertz for the suction side, and from 700 to 520 for the pressure side. The frequency and wavenumber ranges are obtained by using a database method.[52] For each wave, the modes obtained from the database method are analyzed in our LST framework in order to determine the neutral point locations. For flight condition 2, however, transition in the lower side of the airfoil is found to be caused by an LSB,

differing from all the other situations in which the amplification of TS waves triggers transition to turbulence.

Figure [5] shows the N-envelopes for both flight conditions. For flight condition 2, the N-envelope is not shown for the pressure side since transition takes place by means of an LSB for this case. Table [4] indicates the numerical

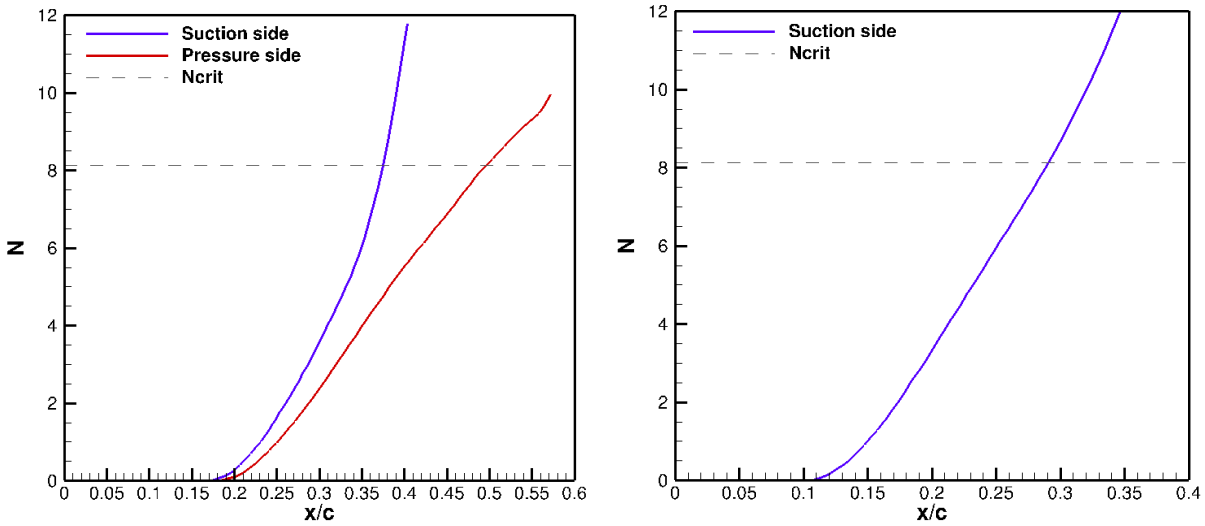

(a) Flight condition 1

(b) Flight condition 2

Figure 5: N-factor envelopes for condition 1 (left) and condition 2 (right) for the NLF(1)-0416 test case.

and experimental transition locations for this test case. The experimental transition locations in Ref. [25] are obtained through the use of acoustic devices that do not precisely detect transition. Instead, this method suggests bounds inside which transition takes place. Then, a curve is fitted, passing inside the bounding regions, in order to indicate the likely transition location. The experimental results shown in Fig. [4] are based on this curve. This approach certainly inputs some additional uncertainty on the transition location placing.

Table 4: NLF(1)-0416 airfoil transition information.

Condition, side	PSE, $(x/c)_{tr}$	Experiment, $(x/c)_{tr}$	Percent Error
1, upper	0.375	0.385	2.56
1, lower	0.497	0.525	5.34
2, upper	0.291	0.310	6.03
2, lower	0.570	0.640	10.85

Despite of the uncertainties involved with the experimental transition location, the results provided by our PSE implementation are in good agreement with experimental data. For the airfoil pressure side in flight condition 2, the larger mismatch between numerical and experimental result follows the trend that linear stability analysis tools tend to predict transition caused by LSBs upstream of its experimental location. Indeed, the way a separation bubble is accounted for in this type of framework involves the divergence of the boundary layer code. Boundary layer calculations involve a marching, hence they represent a parabolic problem whose underlying hypotheses are similar to the ones considered for the PSE approach. When the flow separates, the slow streamwise variation hypothesis does not hold, and the marching procedure diverges. Correlations indicated in Ref. [24] provide a tool to estimate the transition region when separation is involved.

V. Transitional Flow Results in a Discontinuous Galerkin RANS framework

We propose the use of PSE as the transition location prediction tool in a Discontinuous Galerkin RANS implementation. This framework is such that the advantages of a low-dissipation, adaptive CFD framework can be used to simulate transitional flows at high Reynolds numbers, in contrast to techniques such as ILES, that are restricted to low to moderate Reynolds numbers.

V.A. NACA 0012

In order to first verify the concepts presented in Sec. [III], we use the NACA 0012 airfoil results presented in Sec. [IV] with Reynolds numbers of 5 and 15 million, both for M=0.1 and zero angle of attack.

In the numerical simulations we use DG with approximation order $p = 2$ on meshes adapted via adjoint-based output error estimates. An unstructured mesh optimization algorithm through error sampling and error synthesis (MOESS)[53,54] is adopted to capture the highly anisotropic physics in the boundary layer with moderate degrees of freedom (DOF). In this paper, our meshes are adapted for the drag output only, given that this is the aerodynamic coefficient most affected by the transition inclusion. The starting and final computational meshes are depicted in Fig. [6].

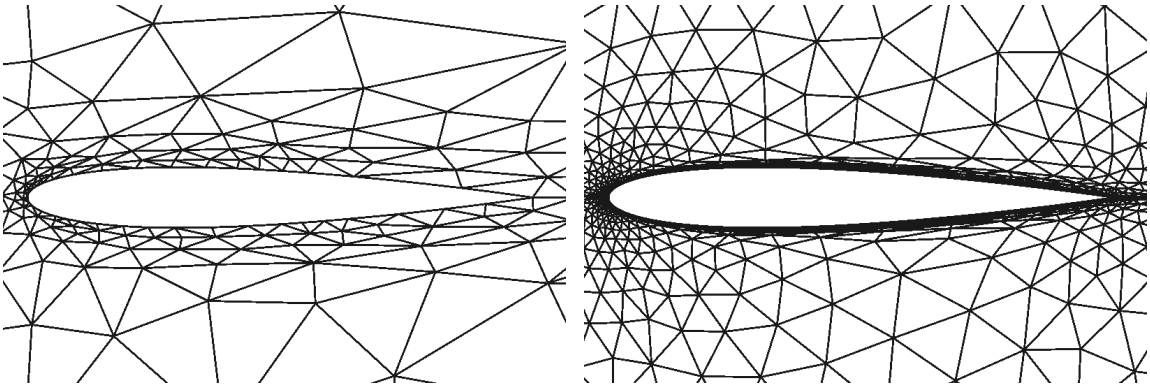

(a) Initial mesh. DOF = 3198 (b) Adapted mesh. DOF = 41190

Figure 6: Examples of initial and adapted meshes for a NACA 0012 run.

Figure [7] shows contours of $\tilde{\nu}$, the SA model working variable and directly related to the kinetic eddy viscosity, for the 5 million Reynolds test case for both fully turbulent and including transition to turbulence simulations. It is evident that our implementation is able to turn off the turbulence effects ahead of the transition region. After this position, predicted by PSE, the intermittency function from Eq. [22] is used to turn on the turbulence production and destruction terms.

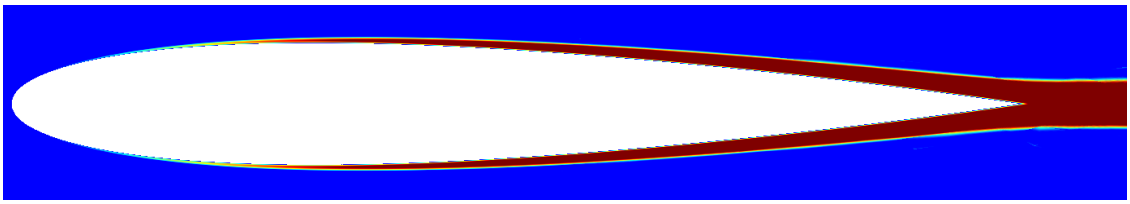

(a) Fully turbulent

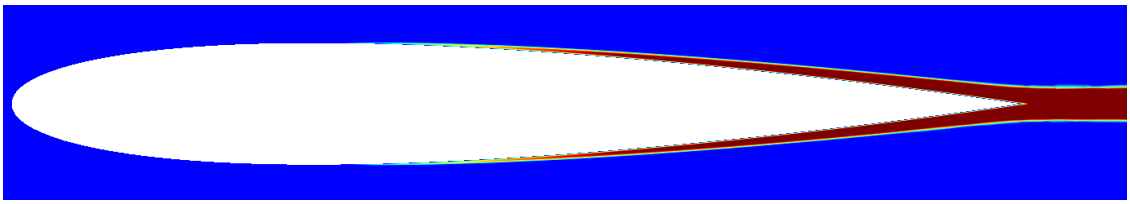

(b) Transition included

Figure 7: SA model working variable $\tilde{\nu}$ contours for the NACA 0012 case at Re=5 million for a fully turbulent simulation (top) and including transitional effects (bottom). The contour range is from 0 to 0.02.

The effects of transition on the pressure coefficient distribution can be seen in Fig. [8]. The overall c_p distribution looks very similar for both turbulent and transitional test cases, which seems to be physical as no shock waves are present in this test case. By zooming in on the c_p curve around the transition region, however, we observe that the

transitional flow case presents some small differences with respect to the turbulent case in this region.

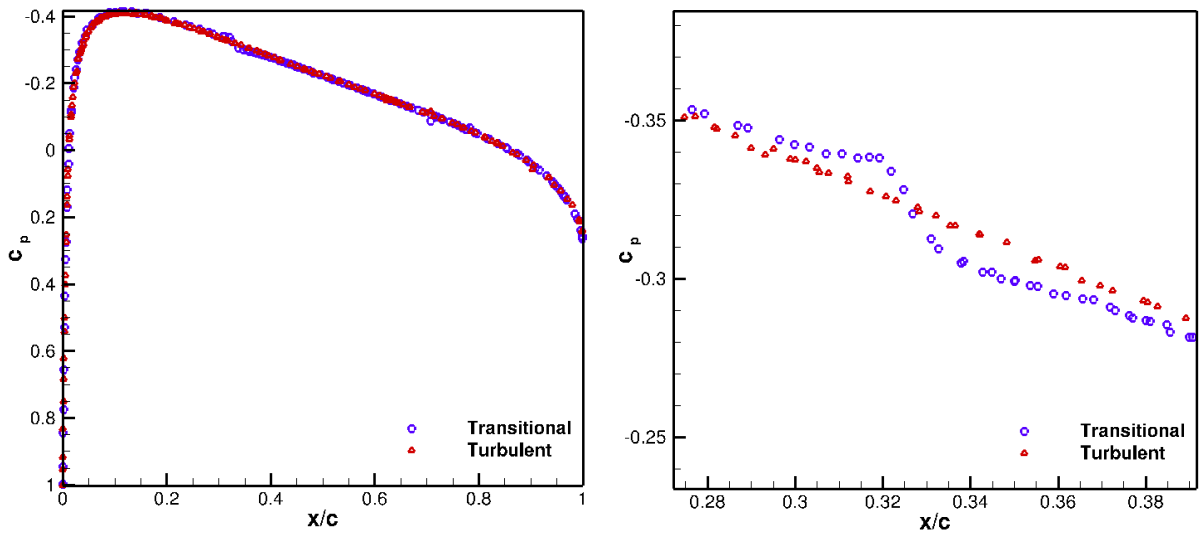

(a) c_p, overview

(b) c_p, zoom-in around the transition region

Figure 8: Pressure coefficient distributions. General view (left) and zoomed-in image around the transition region (right) for the NACA 0012 case with Re=5 million.

To better observe the transition location for the NACA 0012 upper surface at Re=5 million, we observe the skin friction coefficient, c_f, plots for both fully-turbulent and transitional simulations. The results are depicted on the left of Fig. [9]. The inclusion of a laminar region, followed by a transitional length, in the simulation leads to a smaller skin friction coefficient, as expected. In addition, the c_f rise around $(x/c) = 0.3$ is another indication that transition, predicted to start at $(x/c) = 0.33$ by our PSE approach, is being correctly reproduced within the RANS framework. Inspection of the skin friction plot shows that some points seem to be off the curve. This is likely due to the discontinuous nature of the DG approach.

Also in Fig. [9] we illustrate, for the transitional flow case, the streamwise velocity component, U, in three different chord-wise positions. First, the velocity profile in the laminar region is representative of laminar flow. As long as turbulence starts being generated in the boundary layer, the enlarged momentum transfer causes the boundary layer velocity profile to become flatter, as we show in Fig. [9]. The relevance of these analyses is that we assure that the interaction between the transition prediction framework and the CFD capability is such that the physical aspects of laminar, transitional, and turbulent flows are retained during the simulation process.

Results for lift, drag, and moment coefficient (around c/4) are indicated in Table [5] for both flight conditions, namely with Reynolds numbers of 5 and 15 million. We highlight that, by including transition effects, the drag is

Table 5: NACA 0012 aerodynamic coefficients.

Case	c_l	c_d	c_m
Re = 5×10^6, Turbulent	-0.000922	0.00864	0.000189
Re = 5×10^6, Transitional	-0.000438	0.00602	0.000129
Re = 15×10^6, Turbulent	-0.000851	0.00749	0.000154
Re = 15×10^6, Transitional	0.000847	0.00603	0.000165

reduced by 30% for the 5 million Reynolds case and by 20% in the 15 million Reynolds case. As for the lift coefficient, the larger variation is observed for the lower Reynolds number case. Since the NACA 0012 airfoil is symmetric and we use a zero angle of attack condition, both lift and moment coefficients are small numbers and, thus, it is harder to draw deeper conclusions for the effect of transition over these variables.

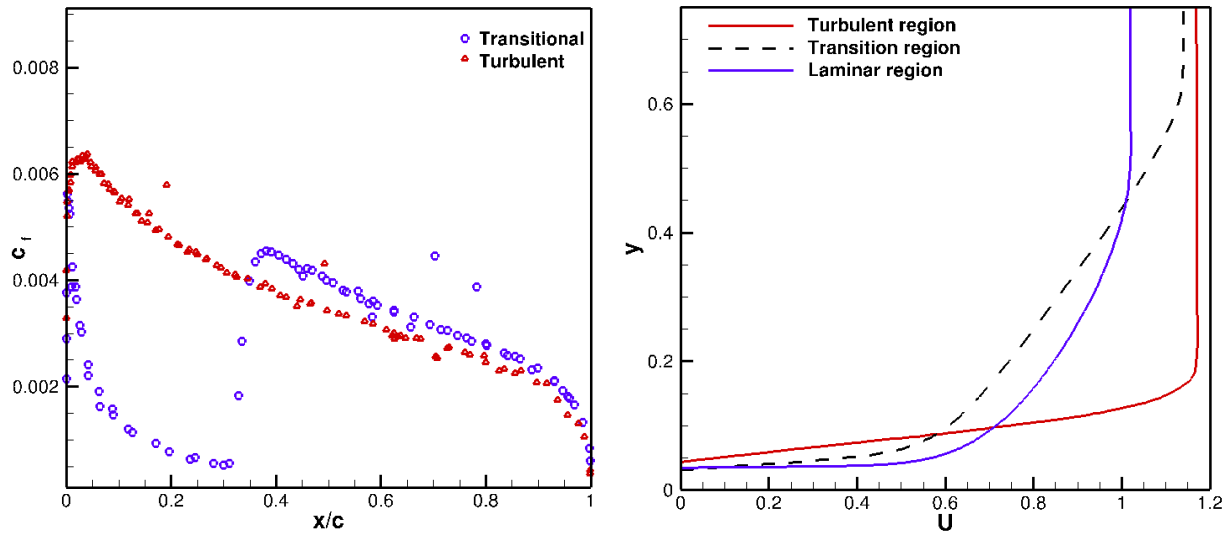

(a) c_f (b) U, transitional flow

Figure 9: NACA 0012 skin friction coefficient for both turbulent and transitional simulations (left) and streamwise velocity in the laminar, transitional, and turbulent regions for the transitional simulation (right) for Re=5 million.

V.B. NLF(1)-0416

Since a considerable amount of experimental data is available for the NLF(1)-0416 airfoil, we use flight conditions 1 (Re=4 million, M=0.1, and zero angle of attack) and 2 (Re=2 million, M=0.1, and 4° angle of attack) from Sec. [IV] to assess both the fully-turbulent and transitional flows for this specific geometry. The starting and final computational meshes are depicted in Fig. [10].

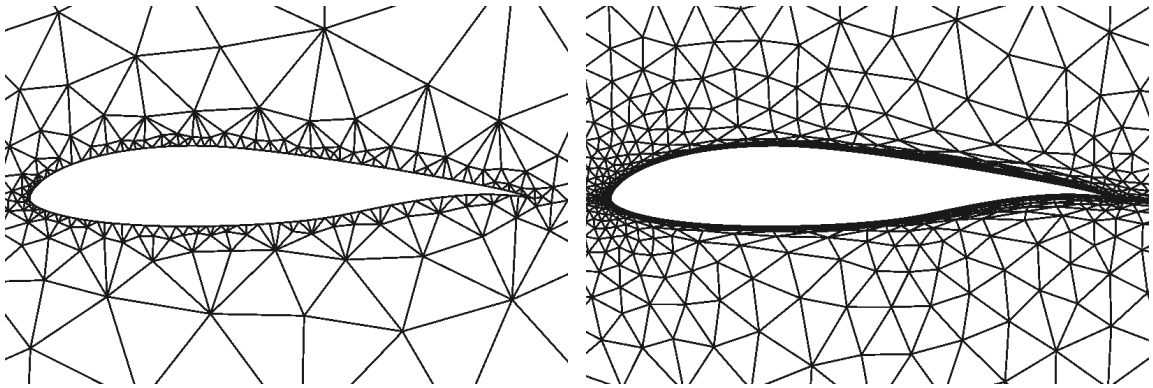

(a) Initial mesh. DOF = 3516 (b) Adapted mesh. DOF = 41484

Figure 10: Examples of initial and adapted meshes for a NLF(1)-0416 run.

Figure [11] shows contours of $\tilde{\nu}$ for condition 1 for both fully turbulent and including transition to turbulence simulations. Here, for a non-symmetric, thicker than the NACA 0012 airfoil, it is even easier to observe the effects of the intermittency function over the SA model turbulent variables.

The pressure coefficient distributions for the turbulent simulation, the transitional simulation, and the experimental data can be seen in Fig. [12]. We observe that both fully-turbulent and transitional flow simulations present a good agreement with c_p from experimental data. For the airfoil pressure side, the fully-turbulent simulation leads to better agreement with experimental data, the transitional flow run leading to better agreement in the suction side. Once again, inspection of the upper surface transition region, predicted to take place between $(x/c) = 0.375$ and $(x/c) = 0.446$, introduces features that are representative of the experimental pressure coefficient distribution, namely a slight, abrupt

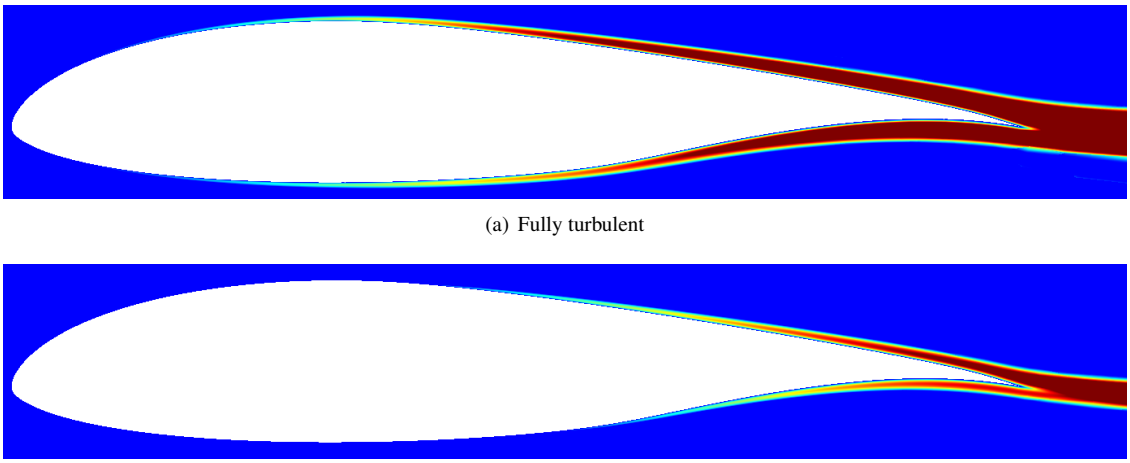

(a) Fully turbulent

(b) Transition included

Figure 11: SA model working variable $\tilde{\nu}$ contours for the NLF(1)-0416 case at Re=4 million for a fully turbulent simulation (top) and including transitional effects (bottom). The contour range is from 0 to 0.03.

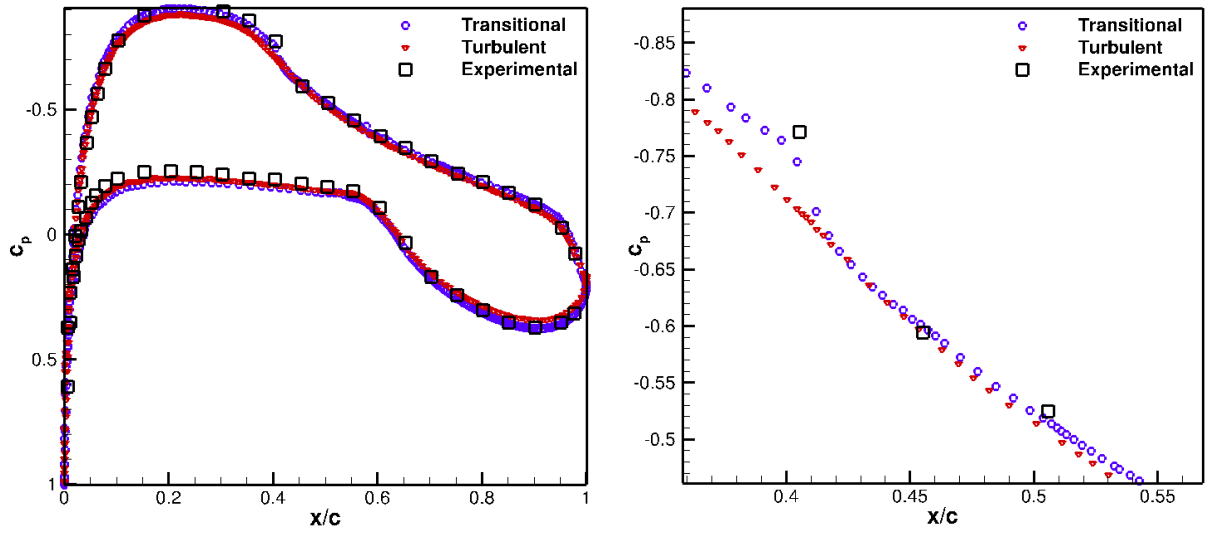

(a) c_p, overview

(b) c_p, zoom-in around the suction side transition region

Figure 12: Pressure coefficient distributions. General view (left) and zoomed-in image around the suction side transition region (right) for flight condition 1, NLF(1)-0416.

increase in the c_p values around the transition region.

Figure [13] shows the skin friction coefficient, c_f, for both turbulent and transitional simulations. Besides the larger c_f values for the turbulent case, as expected, it is interesting to observe that, even in the turbulent region, the c_f computations vary between turbulent and transitional analyses. This is a result from the convective nature of the boundary layer that introduces history effects in this type of flow. As a result, the turbulent boundary layer that, in the early chord positions, was laminar, has a development that is distinct from the one observed in the fully-turbulent case.

Also depicted in Fig. [13] are the streamwise velocity plots for the upper surface, in condition 1, for both laminar, transitional, and turbulent regions. As for the NACA 0012 case, we can observe that our implementation effectively computes boundary layer velocity profiles that are in agreement with the expectation of an increased momentum transfer leading to flatter velocity profiles in the turbulent flow regime.

Table [6] introduces the aerodynamic coefficient results for transitional and turbulent simulations and compares them to the experimental data. We observe that, by including transition to turbulence effects, the percent error in

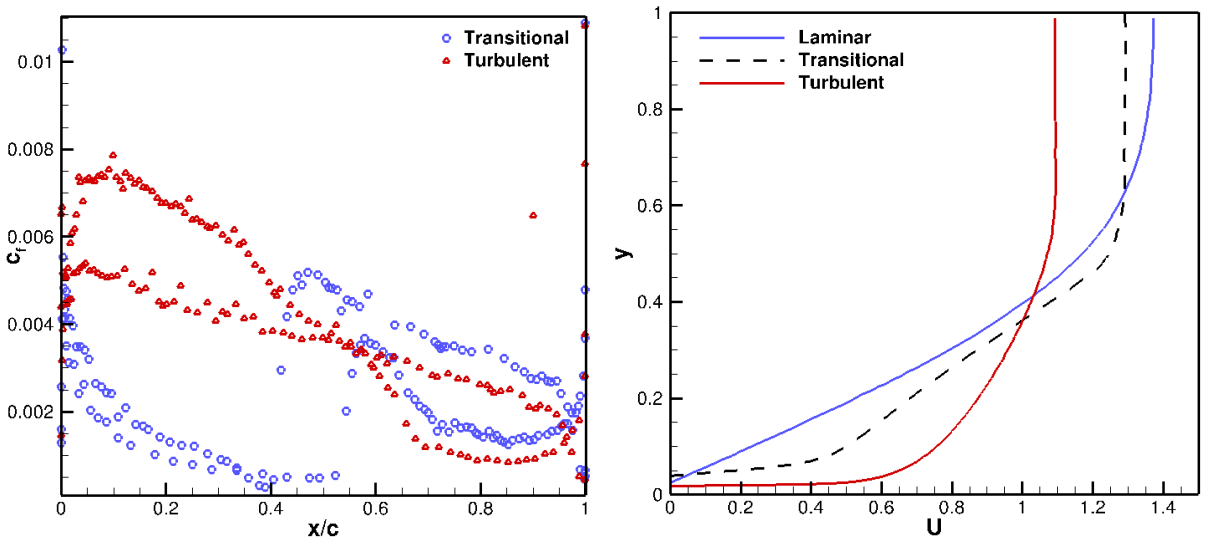

(a) c_f

(b) U, transitional flow. Suction side

Figure 13: NLF(1)-0416 skin friction coefficient for both turbulent and transitional simulations (left) and streamwise velocity in the laminar, transitional, and turbulent regions for the transitional simulation (right) for the suction side at Re=4 million, M=0.1, and zero angle of attack (condition 1).

Table 6: NLF(1)-0416 aerodynamic coefficients for condition 1.

Case	c_l	c_l % error	c_d	c_d % error	L/D	L/D % error	c_m	c_m % error
Turbulent	0.450	0.75	0.0099	68.65	45.26	40.26	-0.0995	4.36
Transitional	0.486	8.86	0.0055	6.18	87.91	16.03	-0.108	3.75
Experiment	0.447	-	0.0059	-	75.76	-	-0.104	-

the drag coefficient prediction drops by one order of magnitude when compared to the fully-turbulent test case. The lift coefficient is overpredicted by the transitional simulations. This trend was also observed by Coder.[49] For the L/D ratio, the transitional simulations are able to better reproduce the experimental value, even though the error is still considerable due to the lift coefficient being overpredicted when transitional effects are included. The moment coefficient around (c/4) presents very similar errors for both turbulent and transitional analyses.

Figure [14] shows $\tilde{\nu}$ contours for condition 2 (Re=2 million, M=0.1, and 4° angle of attack) for both fully turbulent and including transition to turbulence simulations. The intermittency function effect over the turbulence variables can once again be observed. At a higher angle of attack, condition 2 is the best condition, among the ones addressed in this paper, to visualize the $\tilde{\nu}$ topology in both transitional and turbulent cases.

The pressure coefficient distributions for both turbulent simulation, transitional simulation, and experimental data can be seen in Fig. [15]. For flight condition 2, the differences in the c_p curves as obtained by turbulent and transitional simulations are more observable than for flight condition 1, especially close to the suction peak. In the pressure side with transition, we highlight that, close to $(x/c) = 0.6$, a separation region is partially detected by the simulation. This is represented by the almost vertical pressure coefficient portion in the aforementioned chord position. This separation is not captured by the fully turbulent simulation. This has the physical interpretation that a turbulent boundary layer is more resistant to separation than a laminar one.

Figure [16] shows the skin friction coefficient, c_f, for both turbulent and transitional simulations. In agreement with Fig. [15], the c_f value close to zero around $(x/c) = 0.6$ correlates well with the laminar separation bubble that triggers transition in the experimental framework. Once again, the velocity profiles depicted in [16] allow for a clear distinction between laminar, transitional, and turbulent flow regions in the suction side of the airfoil.

Table [7] introduces the aerodynamic coefficient results for transitional and turbulent simulations and compares them to the experimental data. For flight condition 2, the inclusion of transition to turbulence effects improves the drag coefficient prediction, as well as the L/D calculation, leading to results that are very close to experimental data. The

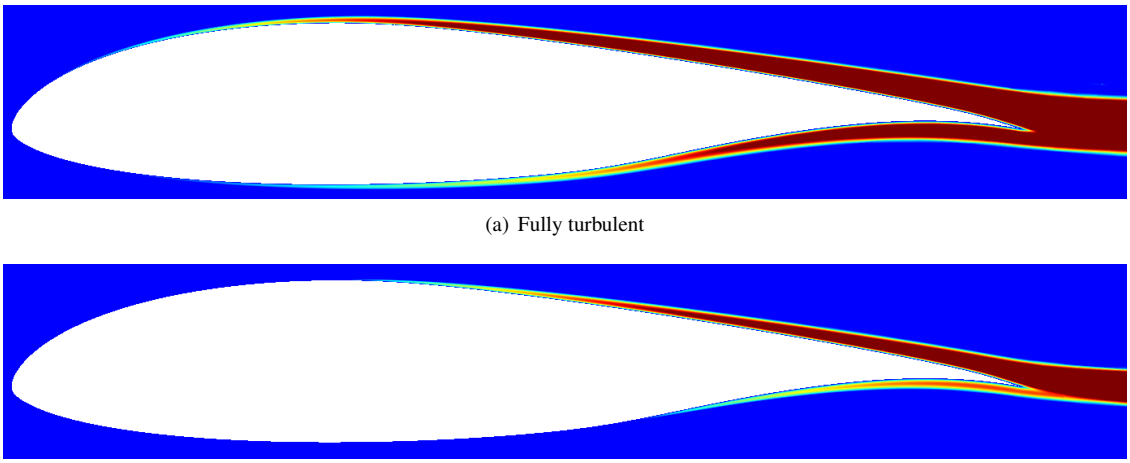

(a) Fully turbulent

(b) Transition included

Figure 14: SA model working variable $\tilde{\nu}$ contours for the NLF(1)-0416 case at Re=2 million for a fully turbulent simulation (top) and including transitional effects (bottom). The contour range is from 0 to 0.03.

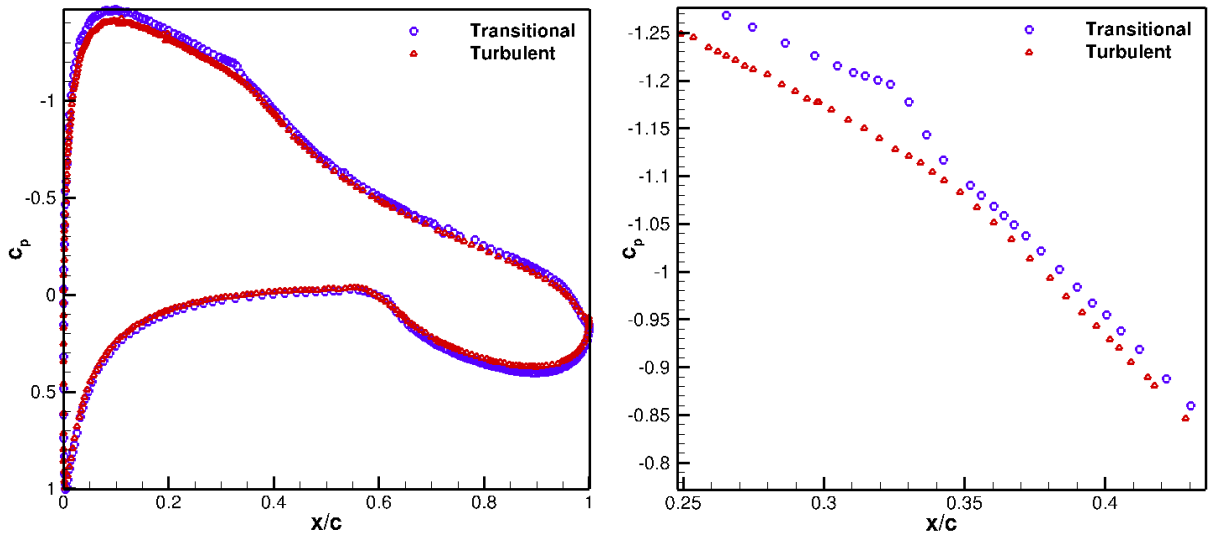

(a) c_p, overview

(b) c_p, zoom-in around the suction side transition region

Figure 15: Pressure coefficient distributions. General view (left) and zoomed-in image around the suction side transition region (right) for flight condition 2, NLF(1)-0416.

Table 7: NLF(1)-0416 aerodynamic coefficients for condition 2.

Case	c_l	c_l % error	c_d	c_d % error	L/D	L/D % error	c_m	c_m % error
Turbulent	0.889	1.07	0.0126	61.09	70.79	37.26	-0.0999	0.11
Transitional	0.937	6.53	0.0077	1.56	122.09	8.21	-0.109	9.19
Experiment	0.880	-	0.0078	-	112.82	-	-0.100	-

lift coefficient, however, is once more overpredicted by the inclusion of transition to turbulence effects.

It is worth mentioning that the NLF(1)-0416 experimental results might suffer from wall effects in the wind tunnel facility and our numerical results do not account for this. Also, there is no experimental information regarding the transition front in different spanwise locations. Checking this point is relevant in order to assure that the experimental

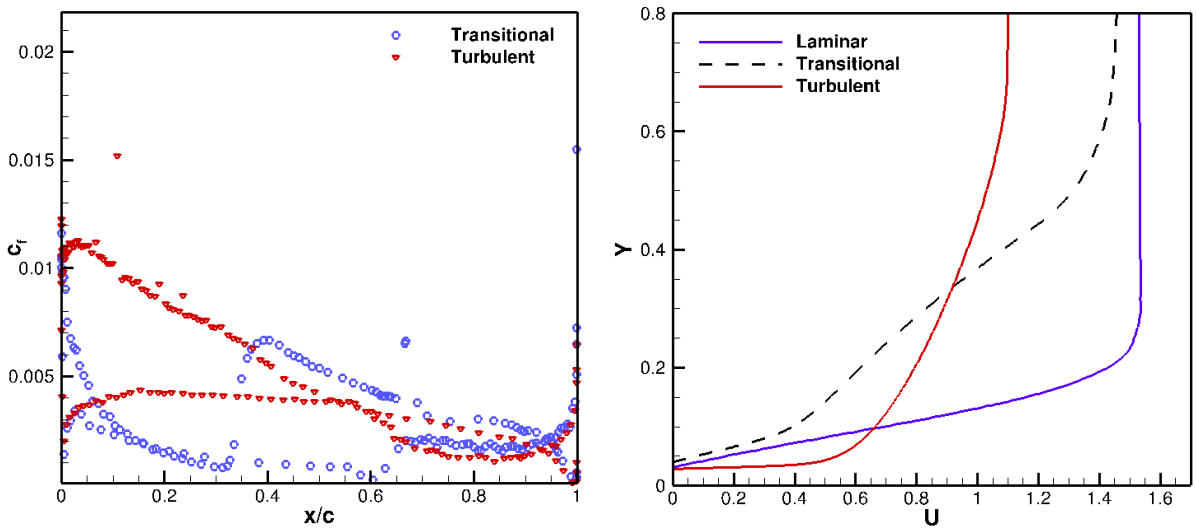

(a) c_f

(b) U, transitional flow. Suction side

Figure 16: NLF(1)-0416 skin friction coefficient for both turbulent and transitional simulations (left) and streamwise velocity in the laminar, transitional, and turbulent regions for the transitional simulation (right) for the suction side at Re=2 million, M=0.1, and 4° angle of attack (condition 2).

results are not suffering three-dimensional effects.

VI. Concluding Remarks

In this paper, we successfully demonstrate that the inclusion of transition to turbulence effects in a RANS framework improves the agreement with experimental data. Our approach is unique in that it introduces laminar and transitional flow areas in a CFD code that uses a Discontinuous-Galerkin discretization. The fact that both nonlocal and nonparallel effects are included in the transition module allows for accurate prediction of transition in boundary layer flows. The framework is targeted at solving high Reynolds number, transitional aerodynamic flows.

The main advantage of the PSE method with respect to local stability analysis tools is that it provides the possibility of accounting for the boundary layer growth. In the classical PSE method, variations in the baseflow strongly occur in the wall-normal direction and weakly in the streamwise direction. We introduce the PSE formulation and highlight the hypotheses that are considered behind the methodology. Our PSE implementation is then verified using a code-to-code verification process. This stage is used to verify both the flow stability calculation and the transition prediction capability. The kinetic energy-based growth rates are compared to those obtained with a benchmark implementation. This is accomplished for both subsonic and supersonic flows over flat plates, considering oblique and aligned TS waves. Two airfoil test cases are also considered. Transition results for a NACA 0012 test case at different Reynolds numbers, as well as for the NLF(1)-0416 airfoil, indicate that our PSE framework is able to correctly handle transition triggered by amplification of TS waves. Experimental results are also used for validation purposes.

By means of a continuous, smooth intermittency function, we are able to turn off production and destruction turbulence terms in the SA turbulence model. By doing so, transition to turbulence effects are accounted for in a RANS framework. We demonstrate that, by including transition to turbulence in our RANS, high order framework, the drag coefficient becomes more accurate than the one obtained by using its fully-turbulent counterpart. The lift coefficient tends to be overpredicted by the inclusion of transition effects, but the efficiency ratio (L/D) becomes better correlated to experimental data.

The interest of including laminar-turbulent transition effects in daily CFD simulations lies not only in the quest for lower drag airframes. In general, even small portions of laminar region that might be present in several flight conditions, may affect the ability to correctly predict several aerodynamic characteristics. This has effects on design areas such as aerodynamics, performance, and flight mechanics. In that sense, using an adaptive, high-order RANS framework along with a PSE-based transition capability paves the way for higher-fidelity design and optimization.

Acknowledgments

The authors gratefully acknowledge the support provided by Conselho Nacional de Desenvolvimento Científico e Tecnológico, CNPq, Brazil, under Research Grant No. 205552/2014-5. The authors also thank Prof. Ardeshir Hanifi (KTH) for the insightful discussions on the PSE approach and for assisting us with our PSE implementation verification.

References

[1]Crouch, J. D. and Ng, L. L., "Variable N-Factor Method for Transition Prediction in Three-Dimensional Boundary Layers," *AIAA Journal*, Vol. 38, No. 2, Feb. 2000, pp. 211–216.

[2]Arnal, D., "Practical Transition Prediction Methods: Subsonic and Transonic Flows," Advances in Laminar Turbulent Transition Modeling. The Lecture Series of the von Karman Institute, 2008.

[3]Deyhle, H. and Bippes, H., "Disturbance Growth in an Unstable Three-Dimensional Boundary Layer and its Dependence on Environmental Conditions," *Journal of Fluid Mechanics*, Vol. 316, 1996, pp. 73–113.

[4]Lynde, M. N. and Campbell, R. L., "Computational Design and Analysis of a Transonic Natural Laminar Flow Wing for a Wind Tunnel Modell," AIAA Paper No. 2017-3058*, Proceedings of the 35th AIAA Applied Aerodynamics Conference, AIAA AVIATION Forum*, Denver, CO, Jun. 2017.

[5]Gaster, M. and Jiang, F., "A Rapid Scheme for Estimating Transition on Wings by Linear Stability Theory," *Proceedings of the 19th Congress of the International Council of Aeronautical Sciences*, 1994.

[6]van Ingen, J. L., "Some Introductory Remarks on Transition prediction Methods based on Linear Stability Theory," *Proceedings of the colloquium Transitional Boundary Layers in Aeronautics*, R. A. W. M. Henkes and J. L. van Ingen ed., Amsterdam, 1996.

[7]Stock, H. and Haase, W., "Some Aspects of Linear Stability Calculations in Industrial Applications," *Proceedings of the colloquium Transitional Boundary Layers in Aeronautics*, R. A. W. M. Henkes and J. L. van Ingen ed., Amsterdam, 1996.

[8]Crouch, J. D., Crouch, I. W. M., and Ng, L. L., "Transition Prediction for Three-Dimensional Boundary Layers in Computational Fluid Dynamics Applications," *AIAA Journal*, Vol. 40, No. 8, Aug. 2002, pp. 1536–1541.

[9]Drela, M., "Implicit Implementation of the Full eN Transition Criterion," AIAA Paper No. 2003-4066*, Proceedings of the 21st AIAA Aplied Aerodynamics Conference*, Orlando, FL, Jun. 2003.

[10]Halila, G. L. O., Bigarella, E. D. V., and Azevedo, J. L. F., "A Numerical Study on Transitional Flows Using a Correlation-Based Transition Model," *Journal of Aircraft*, Vol. 53, No. 4, Jul.–Aug. 2016, pp. 922–941.

[11]Halila, G. L. O., Bigarella, E. D. V., Antunes, A. P., and Azevedo, J. L. F., "An Efficient Setup for Freestream Turbulence on Transition Prediction over Aerospace Configurations," *Aerospace Science and Technology*, Vol. 81, Oct. 2018, pp. 259–271.

[12]Pasquale, D., Rona, A., and Garret, S. J., "A Selective Review of CFD Transition Models," AIAA Paper No. 2009-3812*, Proceedings of the 39th AIAA Fluid Dynamics Conference*, San Antonio, TX, June 2009.

[13]Uranga, A., Persson, P. O., Drela, M., and Peraire, J., "Implicit Large Eddy Simulation of Transition to Turbulence at low Reynolds Numbers using a Discontinuous Galerkin Method," *International Journal for Numerical Methods in Engineering*, Vol. 87, Oct. 2010, pp. 232–261.

[14]Fernandez, P., Nguyen, N., and Peraire, J., "The Hybridized Discontinuous Galerkin Method for Implicit Large-Eddy Simulation of Transitional Turbulent Flows," *Journal of Computational Physics*, Vol. 336, 2017, pp. 308–329.

[15]Zheng, X., Liu, C., and Yang, C., "Turbulent Transition Simulation Using the $k-\omega$ Model," *International Journal for Numerical Methods in Engineering*, Vol. 42, 1998, pp. 907–926.

[16]Juniper, M. P., Hanifi, A., and Theofilis, V., "Modal Stability Theory. Lecture notes from the FLOW-NORDITA Summer School on Advanced Instability Methods for Complex Flows. Stockholm, Sweden, 2013," *Aplied Mechanics Reviews*, Vol. 66, Mar. 2014, pp. 1–22.

[17]Saric, W. S., "Introduction to Linear Stability," Advances in Laminar Turbulent Transition Modeling. The Lecture Series of the von Karman Institute, 2008.

[18]Bertolotti, F. P. and Herbert, T., "Analysis of the Linear Stability of Compressible Boundary Layers using PSE," *Theoretical and Computational Fluid Dynamics*, , No. 3, 1991, pp. 117–124.

[19]Bertolotti, F. P., Herbert, T., and Spalart, P. R., "Linear and Nonlinear Stability of the Blasius Boundary Layer," *Journal of Fluid Mechanics*, , No. 242, 1992, pp. 441–474.

[20]Herbert, T., "Parabolized Stability Equations," *Annual Review of Fluid Mechanics*, , No. 29, 1997, pp. 245–283.

[21]Kosarev, L., Séror, S., and Lifshitz, Y., "Parabolized Stability Equations Code with Automatic Inflow for Swept Wing Transition Analysis," *Journal of Aircraft*, Vol. 53, No. 6, Nov.-Dec. 2016, pp. 1647–1669.

[22]Arnal, D., "Boundary layer Transition: Predictions based on the Linear Theory," AGARD Report AG 793, Apr. 1994.

[23]van Ingen, J. L., "A Suggested Semi-Empirical Method for the Calculation of the Boundary Layer Transition Region," Univ. Delft Report VTH-74, University of Delft, Delft, The Nederlands, 1956.

[24]Shi, Y., Gross, R., Mader, C. A., and Martins, J. R. R. A., "Transition Prediction Based on Linear Stability Theory with the RANS Solver for Three-Dimensional Configurationsl," AIAA Paper No. 2018-0819*, Proceedings of the 2018 AIAA Aerospace Sciences Meeting, AIAA SciTech Forum*, Kissimmee, FL, Jan. 2018.

[25]Somers, D. M., "Design and Experimental Results for a Natural-Laminar-Flow Airfoilfor General Aviation Applications," NASA TP-1981-1861, NASA, Jun. 1981.

[26]Hicks, R. M., Murman, E. M., and Vanderplaats, G. N., "An Assessment of Airfoil Design by Numerical Optimization," NASA TM-x-3092, NASA, 1974.

[27]Pironneau, O., "On Optimum Profiles in Stokes Flow," *Journal of Fluid Mechanics*, Vol. 59, No. 1, 1973, pp. 117–128.

[28]Pironneau, O., "On Optimum Design in Fluid Mechanics," *Journal of Fluid Mechanics*, Vol. 59, No. 1, 1974, pp. 97–110.

[29]Jameson, A., "Aerodynamic Design via Control Theory," *Journal of Scientific Computing*, Vol. 3, No. 3, 1988, pp. 233–260.

[30]Lyu, Z., Kenway, G. K. W., and Martins, J. R. R. A., "Aerodynamic Shape Optimization Investigations of the Common Research Model Wing Benchmark," *AIAA Journal*, Vol. 53, No. 4, April 2015, pp. 968–985.

[31]Chen, S., Lyu, Z., Kenway, G. K. W., and Martins, J. R. R. A., "Aerodynamic Shape Optimization of Common Research Model Wing–Body–Tail Configuration," *Journal of Aircraft*, Vol. 53, No. 1, Jan-Feb 2016, pp. 276–293.

[32]Chen, G. and Fidkowski, K. J., "Airfoil Shape Optimization Using Output-Based Adapted Meshes," AIAA Paper No. 2017-3102*, Proceedings of the 23rd AIAA Computational Fluid Dynamics Conference,*, Denver, CO, Jun. 2017.

[33]Allmaras, S. R. and Johnson, F. T., "Modifications and Clarifications for the Implementation of the Spalart-Allmaras Turbulence Model," *Seventh International Conference on Computational Fluid Dynamics (ICCFD7)*, 2012, pp. 1–11.

[34]Baumann, C. E. and Oden, J. T., "A Discontinuous hp Finite Element Method for Convection-diffusion Problems," *Computer Methods in Applied Mechanics and Engineering*, Vol. 175, No. 3, 1999, pp. 311 – 341.

[35]Houston, P. and Süli, E., "HP-adaptive Discontinuous Galerkin Finite Element Methods for First-Order Hyperbolic Problems," *SIAM Journal on Scientific Computing*, Vol. 23, No. 4, 2001, pp. 1226–1252.

[36]Wang, L. and Mavriplis, D. J., "Adjoint-based h-p Adaptive Discontinuous Galerkin Methods for the 2D Compressible Euler Equations," *Journal of Computational Physics*, Vol. 228, No. 20, 2009, pp. 7643 – 7661.

[37]Roe, P. L., "Approximate Riemann Solvers, Parameter Vectors, and Difference Schemes," *Journal of computational physics*, Vol. 43, No. 2, 1981, pp. 357–372.

[38]Bassi, F. and Rebay, S., "GMRES Discontinuous Galerkin Solution of the Compressible Navier-Stokes Equations," *Discontinuous Galerkin Methods*, Springer, 2000, pp. 197–208.

[39]White, F. M., *Viscous Fluid Flow*, McGraw-Hill, New York, NY, 1991.

[40]Schmid, P. and Henningson, P., *Stability and Transition in Shear Flows*, Springer, New York, 2001.

[41]Bertolotti, F. B., *Linear and Nonlinear Stability of Boundary Layer with Streamwise Varying Properties*, Ph.D. Thesis, The Ohio State Univeristy, Columbus, OH, 1991.

[42]Bertolotti, F. P., *Turbulence and Transition Modelling. Ch. 8, Transition Modelling based on the PSE*, Kluwer Academic Publishers, Netherlands, 1996.

[43]Hanifi, A., Henningson, D., Hein, S., Bertolotti, F., and Simen, M., "Linear Nonlocal Instability Analysis — the linear NOLOT code," The aeronautical research institute of sweden aerodynamics department, FFA-TN 1994-54, 1994.

[44]Andersson, P., Henningson, D. S., and Hanifi, A., "On a Stabilization Procedure for the Parabolic Stability Equations," *Journal of Engineering Mathematics*, Vol. 33, Feb. 1998, pp. 311–332.

[45]Chang, C. L., "LASTRAC.3d: Transition Prediction in 3D Boundary Layers," AIAA Paper No. 2004-2542*, Proceedings of the 34th AIAA Fluid Dynamics Conference and Exhibit*, Portland, OR, Jun. 2004.

[46]Langlois, M., Casalis, G., and Arnal, D., "On the Practical Applications of the PSE Approach to Linear Stability Analysis," *Aerospace Science and Technology*, , No. 3, 1998, pp. 167–176.

[47]Mack, L. M., "Transition Prediction and Linear Stability Theory," AGARD Report CP224, 1977.

[48]Krumbein, A., "Automatic Transition Prediction and Application to Three-Dimensional Wing Configurations," *Journal of Aircraft*, Vol. 44, No. 1, Jan. 2007, pp. 119–133.

[49]Coder, J. G., *Development of a CFD-compatible Transition Model based on Linear Stability Theory*, Ph.D. Thesis, The Pennsylvania State Univeristy, State College, PA, 2014.

[50]Langtry, R. B. and Menter, F. R., "Correlation-Based Transition Modeling for Unstructured Parallelized Computational Fluid Dynamics Codes," *AIAA Journal*, Vol. 47, No. 12, Dec. 2009, pp. 2894–2906.

[51]von Doenhoff, A. E. and Abbott, F. T., "The Langley Two-Dimensional Low-Turbulence Pressure Tunnel," NACA TN-1947-1283, NACA, May 1947.

[52]Perraud, J., Arnal, D., Casalis, G., Archambaud, J., and Donelli, R., "Automatic Transition Prediction using Simplified Methods," *AIAA Journal*, Vol. 47, No. 11, Nov. 2009, pp. 2676–2684.

[53]Yano, M. and Darmofal, D. L., "An Optimization-based Framework for Anisotropic Simplex Mesh Adaptation," *Journal of Computational Physics*, Vol. 231, No. 22, 2012, pp. 7626–7649.

[54]Fidkowski, K., "A Local Sampling Approach to Anisotropic Metric-based Mesh Optimization," *54th AIAA Aerospace Sciences Meeting*, 2016, p. 0835.